PHYSICAL REVIEW B VOLUME 26, NUMBER 8 15 OCTOBER 1982

Lattice-dynamical model for alkali-metal–graphite intercalation compounds

R. Al-Jishi
Department of Physics and Center for Materials Science and Engineering, Massachusetts Institute of Technology, Cambridge, Massachusetts 02139

G. Dresselhaus
Francis Bitter National Magnet Laboratory, Massachusetts Institute of Technology, Cambridge, Massachusetts 02139

(Received 29 March 1982)

The phonon dispersion curves for graphite intercalation compounds (GIC's) are calculated for the case of potassium, rubidium, and cesium intercalates. The model is based on the staging periodicity in these compounds in that it assumes that the symmetry of the graphite crystal is preserved upon intercalation. The effect of intercalation is, therefore, taken into account by a k_z-axis zone folding of the graphite dynamical matrix. The resulting phonon dispersion curves yield results in agreement with all the reported data on GIC's, derived from neutron scattering and specific-heat measurements, and first- and second-order Raman scattering experiments.

I. INTRODUCTION

Graphite intercalation compounds (GIC's) are formed by introducing atomic or molecular layers of a different chemical species, the intercalate, between the carbon layers of graphite. Such a process results in a c-axis ordering called the staging phenomenon whereby for stage n, there are n consecutive graphite layers followed by an intercalate layer. GIC's can be classified as donors (electrons transferred to carbon layers) or acceptors (holes transferred to carbon layers).

Recently, there has been an increase in experimental activity in connection with the lattice properties of the GIC. Dispersion curves are now available through neutron and Raman scattering experiments[1–7] for [001] longitudinal phonons (i.e., A_1 symmetry modes) for different stages with intercalates K, Rb, and Cs, as well as some planar vibrational modes (i.e., E symmetry modes) connected with the intercalate atoms. Also, it is found that the high-frequency E_{2g_2} and E_{1u} modes are split into graphite bounding- and interior-layer modes.[8–10] First-order Raman spectra show that the E_{2g_2} Raman-active mode frequency is stage dependent. This mode is downshifted for donor compounds and upshifted for acceptor compounds as a function of increasing intercalate concentration.[10–14] Raman scattering has been the principal experimental technique that yields information on the phonon dispersion relations for frequencies above ~ 500 cm^{-1}.

Recently, Raman scattering experiments have been carried out[7,15,16] to probe the phonon modes in the frequency range $10-50$ cm^{-1}, yielding a splitting of these shear phonons into bounding- and interior-layer modes. With increasing stage, the interior shear-mode frequencies are found to approach 42 cm^{-1}, which is the zone-center shear phonon frequency in pristine graphite, whereas the bounding-layer modes are shifted to lower frequencies.

Second-order Raman scattering experiments with frequency shifts in the range $1600 < \omega < 3200$ cm^{-1} on graphite-rubidium intercalation compounds show a definite stage dependence of the position of the peaks for $n \geq 3$, in which the peak position shifts upward with increasing stage n.[14] However, no peaks were observed in the second-order spectra of stages 1 and 2, where there are only graphite bounding layers and no interior layers; on the other hand, peaks were observed in the first-order Raman spectrum for these compounds. In stage-2 donor GIC's, a sharp peak is observed in the first-order Raman spectrum at $\omega \sim 1600$ cm^{-1}, while a broad Breit-Wigner line peaking near 1500 cm^{-1} is observed in stage 1.[17,18] This feature in stage 1 was explained by Eklund and Subbaswammy[19] in terms

of a strong coupling between a discrete graphite mode at frequency $\omega \sim 1585$ cm^{-1} to a frequency-dependent phonon continuum, while Miyazaki *et al.*[20] interpreted this broad feature as a coupling between three discrete phonon modes and a continuum in the electronic states. Finally, specific-heat measurements[21–23] showed an anomalous behavior in stage-1, -2, -3, and -4 graphite-Rb compounds and in C_8Cs, whereas no anomalies were observed for the case of graphite-K compounds in the temperature range of $0 < T < 90$ K. The specific heat anomalies in C_8Rb and C_8Cs were identified with an Einstein temperature.[23]

Lattice-dynamical calculations for GIC's have been sparse. The first calculation was done by Horie *et al.*,[24] who performed a lattice-dynamical calculation for first-stage C_8K and C_8Rb compounds based on the Maeda model[25] for the lattice dynamics of pristine graphite. The Horie calculation gives 54 modes mainly due to zone folding of the in-plane $(2\times 2)R\,0°$ superlattice. More recently, Leung *et al.*[26] developed an approach in which the dispersion curves for all GIC stages can be obtained from those of pristine graphite by carrying out a k_z-axis zone folding of the graphite dynamical matrix and replacing the appropriate carbon layers with intercalate layers. This technique will be used in this work to construct a lattice dynamical model for donor GIC's, which accounts for all the information obtained from the above-mentioned experiments. In particular, the model will relate the charge transferred from the intercalate to the carbon bounding layers with the observed features in the first- and second-order Raman spectra.

The calculation of the phonon-dispersion relations is thus motiviated by the need to explain a large variety of phenomena observed by Raman and infrared spectroscopy[5–18] and inelastic neutron scattering.[1–5] The results of the calculation can then be used to explain anomalies observed in the heat capacity,[21–23] to model electron-phonon scattering, which dominates electrical transport phenomena,[27] and to model phonon-phonon and phonon-defect scattering, which are also important in thermal transport phenomena.[29] In this work, a calculation of the second-order Raman spectrum is presented. The results of this calculation are needed to identify the phonon mode frequencies observed in the second-order spectra[6,29] with specific locations in the Brillouin zone. This calculation of the second-order Raman spectrum is also of intrinsic interest in explaining the suppression of the second-order features in the graphite bounding layers of the alkali-metal donor compounds.[29]

The model can furthermore be extended and applied to the interpretation of phase transitions in the intercalate layer that have recently been observed in the graphite-Br_2 (Ref. 30) and graphite-Rb (Ref. 7) systems. The transition from an incommensurate to a commensurate phase introduces additional in-plane superlattice periodicities that result in the zone folding of specific zone-edge phonon modes into the Brillouin-zone center. Thus Raman scattering experiments can serve to detect such transitions. A detailed knowledge of the phonon-dispersion curves can be used to identify the superlattice structure.[7] The extension of the present model to treat in-plane superlattice structures would involve an in-plane zone folding of the phonon-dispersion relations calculated in this paper for the staged compounds followed by the introduction of a perturbation with the in-plane superlattice symmetry to produce a splitting of the folded modes at the high-symmetry points and axes.

It is found experimentally that the in-plane intercalate structure has only a minor effect on the observed in-plane Raman spectra.[7,30] For this reason, the present calculation does not explictly treat in-plane zone folding. In this way, it is possible to keep the calculation general and applicable to alkali-metal donor compounds with different in-plane orderings.

II. PHONON-DISPERSION CURVES IN GIC's

In this work, the dynamical matrix for GIC's is based on that for pristine graphite developed previously by the authors.[31,32] In that model for pristine graphite, interactions up to the fourth-nearest intra- and interplane neighbors were considered. All data obtained from neutron and Raman scattering, sound-velocity, and infrared-absorption experiments are in good agreement with the results calculated on the basis of the model. Moreover, the second-order Raman spectrum is calculated, and all main features in the observed spectrum can be explained as overtones. In Table I, the force constants for pristine graphite are given, where $\phi_r^{(n)}$, $\phi_t^{(n)}$, and $\phi_{to}^{(n)}$ denote, respectively, the in-plane radial, tangential, and out-of-plane tangential force constants between nth nearest intraplane neighbors. The radial and tangential force constants between nth-nearest interplane neighbors are denoted by $\hat{\phi}_r^{(n)}$ and $\hat{\phi}_t^{(n)}$, respectively.

TABLE I. Values of the force-constant parameters in dyn/cm for pristine graphite.

Radial	Tangential	
$\phi_r^{(1)} = 312\,520.0$	$\phi_{ti}^{(1)} = 267\,480.0$	$\phi_{to}^{(1)} = 86\,545.0$
$\phi_r^{(2)} = 120\,920.0$	$\phi_{ti}^{(2)} = -63\,731.0$	$\phi_{to}^{(2)} = -9312.2$
$\phi_r^{(3)} = 27\,978.0$	$\phi_{ti}^{(3)} = 19\,000.0$	$\phi_{to}^{(3)} = 12\,695.0$
$\phi_r^{(4)} = -25\,508.0$	$\phi_{ti}^{(4)} = 9488.0$	$\phi_{to}^{(4)} = 5498.4$
$\hat{\phi}_r^{(1)} = 2746.9$	$\hat{\phi}_t^{(1)} = -5934.1$	
$\hat{\phi}_r^{(2)} = 595.52$	$\hat{\phi}_t^{(2)} = 1271.2$	
$\hat{\phi}_r^{(3)} = -473.88$	$\hat{\phi}_t^{(3)} = 473.9$	
$\hat{\phi}_r^{(4)} = 200.0$	$\hat{\phi}_t^{(4)} = -927.8$	

In calculating the dynamical matrix for GIC's, the layers stacking *AXAX* . . . is assumed for stage 1, *ABXABX* . . . for stage 2, *ABAXABAX* . . . for stage 3, and *ABABXABABX* . . . for stage 4, where *A* and *B* are graphite carbon layers and *X* is an intercalate layer. For the even stages, a stacking *ABXBAXAB* . . . was assumed previously,[26] resulting in a further folding of the k_z-axis dispersion curves. This additional folding complicates the calculation considerably and leads to only minor changes in the dispersion relations and density of states. In the present calculation for a stage-n GIC, the unit cell is taken to include n carbon layers with two distinct carbon atoms in each layer and one intercalate layer containing a single unit of mass. In order to model a $C_{n\xi}X$ compound the atom of the intercalate layer X is considered to be distributed over the graphite unit cells with $2/\xi$ of an X atom taken as the mass per unit cell. In odd-stage compounds, the intercalate atoms are placed over the center of every graphite hexagon, whereas in even-stage GIC's, the intercalate atoms are placed at the midpoint of the line, normal to the carbon layers, that connects two carbon atoms, one in an *A* layer and the other in a *B* layer, as shown in Fig. 1, which illustrates the layer stacking assumed in this model. To keep the correct intercalate concentration, the mass of the intercalate unit is taken as $\frac{1}{4}$ the intercalate atomic weight in stage-1 compounds and $\frac{1}{6}$ of that for $n \geq 2$ in accordance with the commonly reported stoichiometries of these compounds; C_8X for stage 1 and $C_{12n}X$ for $n \geq 2$. With these assumptions relatively high-stage compounds can be modeled without use of excessive computer time.

It is to be noted that the $C_{2n}X$ intercalate structure does not correspond to any known GIC. The observed Raman spectra, however, are not, in general, senstive to the in-plane structure.[33,34] Thus the in-plane $C_{2n}X$ structure was chosen for the calculation on the basis of computation simplicity and for general applicability to alkali-metal GIC's.

The c-axis periodicity, imposed by the staging superlattice, is taken into account by zone folding the pristine graphite dynamical matrix along k_z to obtain the dynamical matrix of the intercalation compound. We use k_z-axis zone folding because the c-axis superlattice resulting from staging is well documented,[35] whereas experimental lattice spectra do not show, except for a few isolated systems,[7,9,17,30] a dependence on the in-plane structure.[33,34] In accordance with the k_z-axis zone folding scheme, the Brillouin zone is $(n+1)/2$ times smaller than that of graphite for a stage-n intercalation compound. This inverse scaling relation also applies to the k_z-axis reciprocal-lattice vectors.

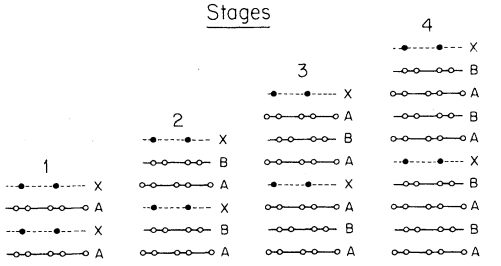

FIG. 1. Schematic diagrams illustrating the atomic arrangements considered in this work for stages $1 \leq n \leq 4$. The intercalate atoms are denoted by solid circles in a layer X. Carbon atoms are indicated by open circles in A and B graphite layers.

The zone-folded dynamical matrix is then transformed into the layer representation through a unitary transformation.[26] In this representation, each layer can be identified with a specific row and column in the dynamical matrix. A graphite layer is then replaced by an intercalate layer, thereby explicitly taking the effect of intercalation into account.

The force constants between in-plane carbon atoms are assumed to be stage dependent in general. In order to fit the stage dependence of the Raman data, it is necessary to introduce stage-dependent force constants defined below. In the graphite layers bounding the intercalate layers, the force constants are taken as

$$\phi=\phi_0(1.04-0.04/n)\ , \tag{1}$$

whereas in the graphite interior layers, the corresponding relation is taken as

$$\phi=\phi_0(1-0.025/n),\quad n\geq 3\ . \tag{2}$$

In Eqs. (1) and (2), ϕ_0 represents the force constant between two atoms in the plane of the carbon layers of pristine graphite. Such a dependence of the force constants on stage index may be explained as follows. Figure 2 shows a qualitative plot of the bonding energy between two atoms in a solid as a function of the bond length. As the two atoms are brought closer, the charge overlap increases, causing a decrease in the energy. At a certain separation, the energy is minimum, beyond which the Coulomb repulsion between the nuclei takes over making the energy increase rapidly. In the case of GIC's, the charge transfer to the carbon bounding layers causes the bond length to expand in order to minimize the free energy.[36] The expansion, however, is shared with the carbon interior layers, giving a stage-dependent carbon—carbon bond length, d_{C-C}, given by[37]

$$d_{C-C}=x_0+l_0/n \tag{3}$$

in which the nearest neighbor C-C distance in pristine graphite is $x_0=1.4203$ Å and $l_0=0.013$ Å. The final situation is thus one in which the C—C bond in bounding carbon layers expands less than what it would normally in order to lie at the potential minimum, the C—C bond in the interior layers expands more than would be expected from the charge transfer to bonds in the graphite interior layers. Both bounding and interior graphite layers are therefore strained for a stage index $n\geq 3$.

Expanding the bonding energy in a Taylor series about the minimum gives

$$V(x)=a(x-x_0)^2-b(x-x_0)^3+c(x-x_0)^4\ , \tag{4}$$

where x_0 is the equilibrium bond length and a, b, and c are taken to be positive. Then the force constant between the two atoms is given by

$$a=\frac{1}{2}\frac{\partial^2 V}{\partial x^2}\ . \tag{5}$$

For $n\geq 3$, the bounding layer d_{C-C} expands by l_0/n to become x_0+l_0/n instead of $x_0+l_0/2$. By assuming that the curvature at the strained equilibrium position x_0+l_0/n is the same as that at this same point in the bonding energy curve whose minimum is at $x_0+l_0/2$, the force constant becomes

$$\phi=\frac{1}{2}\left.\frac{\partial^2 V(x-l_0/2)}{\partial x^2}\right|_{x=x_0+l_0/n} \tag{6a}$$

or

$$\phi=a+3bl_0/2+\tfrac{3}{2}cl_0^2-(3bl_0+6cl_0^2)/n+6cl_0^2/n^2\ . \tag{6b}$$

For large n, the last term in Eq. (6b) becomes negligible, and the same form as in Eq. (1) is obtained. Similar considerations can be applied to the interior layer, giving Eq. (2).

The interlayer force constants between carbon atoms in adjacent carbon layers are taken to be the same as in the case of pristine graphite except for $\hat{\phi}_t$. Comparison to experiment shows that the shear force constants between the layers are reduced by donor intercalation. This is reflected in an increase in $\hat{\phi}_t$. Comparison to experimentally measured low-frequency shear modes[15,16] imply that for

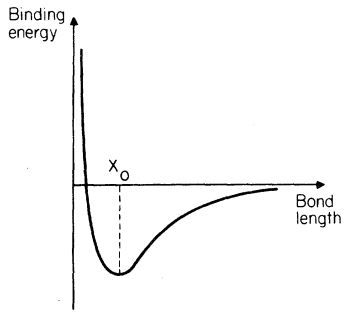

FIG. 2. Diagram illustrating qualitatively the dependence of the energy binding two atoms in a solid on the bond length. The minimum in the potential defines the equilibrium bond length x_0.

TABLE II. Additional force-constant parameters in dyn/cm for K GIC's.

	Stage 1	Stage 2	Stage 3	Stage 4
$\phi_r^{X\text{-}X}$	1400.0	650.0	650.0	650.0
$\phi_t^{X\text{-}X}$	50.0	50.0	50.0	50.0
$\phi_r^{X\text{-}C}$	1660.0	5600.0	1020.0	5600.0
$\phi_t^{X\text{-}C}$	−120.0	85.0	−67.0	70.0
$\phi_{3\text{-}3}^{C}$	100.0	250.0	250.0	250.0

stage-2 GIC's, $\hat{\phi}_t$ is ~ 1.07 times larger than that in Table I and 1.02 times larger in stage-3 GIC. Thus the shear force constants between graphite layers are weaker than in pristine graphite but approach the graphite value with increasing stage.

For this lattice-dynamical model, it is necessary to introduce some additional parameters. These are (a) the radial and tangential components of the intercalate-intercalate force constants $\phi_r^{X\text{-}X}$ and $\phi_t^{X\text{-}X}$, (b) the radial and tangential components of the intercalate-graphite force constants, $\phi_r^{X\text{-}C}$ and $\phi_t^{X\text{-}C}$, and (c) a force constant, $\phi_{3\text{-}3}^{C}$, related to the motion in the z direction of a pair of atoms in the unit cell belonging to the two bounding layers between which the intercalant is sandwiched.

The values of the intercalate-intercalate force constants for stage-1 GIC's are adjusted to reproduce the reported frequencies of the intercalate modes corresponding to planar vibrations of the intercalate atoms.[5] These force constants are taken to be less for $n \geq 2$ than in stage 1 because of the lower in-plane intercalate concentration for alkali-metal compounds with stage index $n \geq 2$.

The intercalate-graphite force constants are chosen such that the longitudinal and shear force constants between the intercalate and the bounding carbon layers are approximately the same for all stages $n \geq 2$. Larger force constants are chosen for stage 1 because of the higher in-plane intercalate concentration for stage 1. The force constant $\phi_{3\text{-}3}^{C}$ is expected to be the same for all stages $n \geq 2$. It is further expected that this force constant in these stages would be larger than in stage 1 because of the higher intercalate concentration in stage 1. These additional parameters are given in Tables II–IV for stages 1, 2, 3, and 4, for K, Rb, and Cs GIC's. These parameters can be used to deduce the values of the force constants for motion of rigid layers in the z direction as well as the shear force constants. In Table V, the c-axis force constants are given for stages for which experimental results were reported. In this table, we introduce an effective interplanar force constant $\Phi(X\text{-}C_b)$, obtained from the observed stiffness $\phi(X\text{-}C_b)$, the c-axis force constant between the intercalate layer and the graphite bounding layer. Values of $\Phi(X\text{-}C_b)$ are obtained by first dividing $\phi(X\text{-}C_b)$ by the pristine graphite stiffness $\phi(C_i\text{-}C_i)$ and then normalizing by division by the relative areal density of the intercalant, $1/\bar{\xi}$, where $\bar{\xi}=\xi/6$.

For stage-1 alkali-metal GIC's, $\bar{\xi}=\frac{4}{3}$ for the assumed atom placements, whereas $\bar{\xi}=2$ for $n \geq 2$. In the notation of Table V, $\phi(C_b\text{-}C_b)$ is the c-axis force constant between the two graphite layers between which the intercalate layer is sandwiched. In Table VI, the shear force constants are given for K GIC. The notation in this table is the same as that in Table V except that the force constants in Table VI are shear force constants rather than c-axis force constants.

It is of interest to note that the Raman scattering results for the low-frequency shear modes[15,16] imply that the shear force constants between adjacent graphite bounding layers are much weaker than for pristine graphite (see Table VI). For the stage $n=3$ compound, the shear force constant between a graphite bounding and graphite interior layer is also reduced but to a lesser degree, and by stage 4, the shear force constant $\phi(C_b\text{-}C_i)$ approaches that of graphite. It is also of interest to note in Table VI

TABLE III. Additional force-constant parameters in dyn/cm for Rb GIC's.

	Stage 1	Stage 2	Stage 3	Stage 4
$\phi_r^{X\text{-}X}$	1300.0	600.0	600.0	600.0
$\phi_t^{X\text{-}X}$	−50.0	−50.0	−50.0	−50.0
$\phi_r^{X\text{-}C}$	1600.0	4800.0	900.0	4800.0
$\phi_t^{X\text{-}C}$	−100.0	85.0	−70.0	85.0
$\phi_{3\text{-}3}^{C}$	0.0	220.0	220.0	220.0

TABLE IV. Additional force-constant parameters in dyn/cm, for Cs GIC's.

	Stage 1	Stage 2	Stage 3	Stage 4
$\phi_r^{X\text{-}X}$	1300.0	600.0	600.0	600.0
$\phi_t^{X\text{-}X}$	−50.0	−50.0	−50.0	−50.0
$\phi_r^{X\text{-}C}$	1600.0	4800.0	900.0	4800.0
$\phi_t^{X\text{-}C}$	−100.0	85.0	−70.0	85.0
$\phi_{3\text{-}3}^{C}$	0.0	220.0	220.0	220.0

that the shear between the intercalant and graphite layers is almost independent of stage.

In Fig. 3 we show the calculated phonon-dispersion curves, along high-symmetry directions for stages 1−4 Rb GIC's, based on this model. The calculated dispersion curves for the corresponding K and Cs compounds for stages $1 \leq n \leq 4$ are qualitatively similar, the similarity being much greater for the high-frequency modes than for the low-frequency modes, which are highly sensitive to the interactions with the intercalant. For stages 1 and 2 there are no graphite interior layers; nevertheless, a small splitting of the nearly degenerate graphite bounding-layer modes is found away from the zone-center. The dominant mode splitting in the dispersion curves for $n=3$ is due to the distinction between the graphite bounding and interior layers, causing a tracking of pairs of phonon branches throughout the Brillouin zone. In this connection it is of interest to note additional small splittings in the dispersion relations for $n=4$ associated with the graphite interior layers away from the zone center. Additional small splittings are also found in the graphite interior-layer modes for higher-stage compounds.[26]

In Fig. 4 we show a plot of the calculated frequencies of the Raman-active E_{2g_2} modes identified with the carbon bounding and interior layers as a function of $1/n$, the reciprocal stage index. This figure shows the good agreement with the experimentally observed values[14] for Rb GIC's of various stages. The model thus accounts for the general downshift of the E_{2g_2} modes with $1/n$ and also the smaller downshift for the interior-layer mode relative to the bounding-layer mode.

The set of force constants for K GIC's given in Table II reproduces the measured low frequencies of the shear phonons.[15] The calculated phonon frequencies along the ΓA direction are compared with the observed values[2] in Fig. 5 for stages $n=1$ and 2 of Rb GIC's, where the agreement is seen to be very good. The same force constants as for stage $n=2$ were used in the calculations for stages 3 and 4 in Fig. 5.

It should be noted that the excellent agreement between the model calculation and the experimental results is due in part to the use of an accurate model for the phonon-dispersion relations for pristine graphite.[32] Most of the force-constant parameters of the present model are fixed by those of pristine graphite and the symmetry of the crystal structure. Further confirmation of the model is provided by the stage independence of the force constants.

The phonon density of states based on these dispersion relations is calculated for different stages of GIC's using the Gilat-Raubenheimer method,[38]

TABLE V. c-axis force constants for the longitudinal modes in K, Rb, and Cs GIC's. The force constants are normalized to those for pristine graphite. A C_8X structure is assumed for the stage-1 compounds and a $C_{12n}X$ structure for the stage-n compounds.

Intercalant	Stage	$\Phi(X\text{-}C_b)$	$\phi(C_b\text{-}C_i)$	$\phi(C_i\text{-}C_i)$	$\phi(C_b\text{-}C_b)$[a]
Potassium	1	1.95		1.0	0.07
	2	1.95	1.0	1.0	0.17
	3	1.80	1.0	1.0	0.17
Rubidium	1	1.87		1.0	0.0
	2	1.68	1.0	1.0	0.15
Cesium	1	1.87		1.0	0.0
	2	1.68	1.0	1.0	0.15

[a]This interaction is between bounding layers across the intercalate layer.

TABLE VI. Shear force constants for K GIC's of various stages. The force constants are normalized to those for pristine graphite.

Stage	$\Phi(X\text{-}C_b)$	$\phi(C_b\text{-}C_i)$	$\phi(C_i\text{-}C_i)$
1	0.19		
2	0.25	0.37	
3	0.28	0.83	
4	0.22	1.0	1.0

and the results are shown in Fig. 6 for graphite-Rb stages $1 \leq n \leq 4$. The density of states of GIC's is found to be similar to that of graphite[31,32] except for three very sharp peaks in the low-frequency range that arise from intercalate modes. These modes occur at higher frequencies for the graphite-K compounds and at lower frequencies for the graphite-Cs compounds, relative to graphite Rb as expected. The high density of states at $\omega \approx 45$ cm^{-1} in stage-1 Rb GIC's suggest that there is an anomaly in the lattice specific heat at a temperature of ~ 65 K, while for $n \geq 2$, the high density of states at $\omega \approx 35$ cm^{-1} predicts an anomalous behavior in the specific heat at $T \sim 50$ K. These predictions are in good agreement with the experimentally observed temperature dependence of the lattice specific heat in graphite-Rb compounds.[21–23]

It should be noted that the results of this work differ in many respects from those of Leung *et al.*[26] Their calculation was based on the Maeda model[25] for pristine graphite and was carried out before many of the GIC data used in the present calculation were known; consequently, the [001] longitudinal and shear phonon frequencies in their calculation[26] were in large error. The frequencies of the modes identified with the intercalate-atom vibrations were calculated[26] to be ~ 600 cm^{-1}, approximately an order of magnitude larger than the experimentally reported values. This difference is manifested in the phonon density of states calculation, where in contrast we here predict three sharp peaks in the range $0 \leq \omega \leq 100$ cm^{-1}.

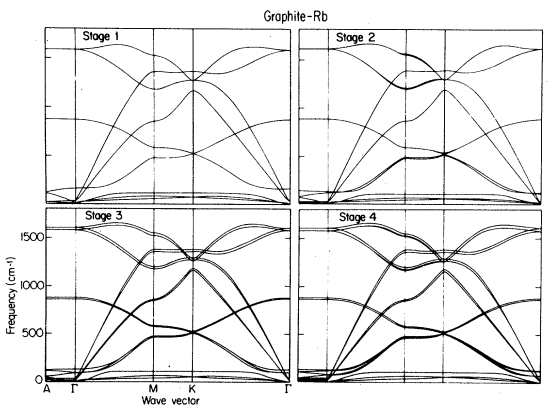

FIG. 3. Phonon-dispersion curves in Rb GIC's for stages 1, 2, 3, and 4, calculated along certain high-symmetry directions using the force constants in Tables I and III (see discussion in text).

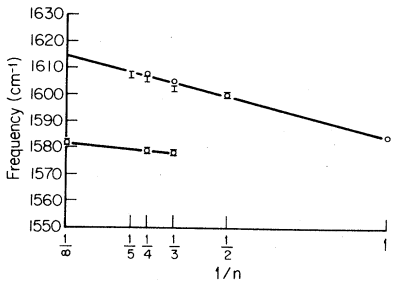

FIG. 4. Raman-active E_{2g_2} mode frequencies in Rb GIC's plotted as a function of $1/n$, the reciprocal of the stage idex. The open circles are the calculated values and the error bars indicate experimental values taken from Ref. 14.

III. RAMAN SCATTERING IN GIC's

A. General considerations

Raman scattering experiments provide a major source of information about the phonon modes for crystals in general and for GIC's in particular. Raman spectra yield the frequencies of the zone-center Raman-active modes as well as the positions of the peaks in the phonon density of states. In first-order Raman scattering, a single zone-center phonon is

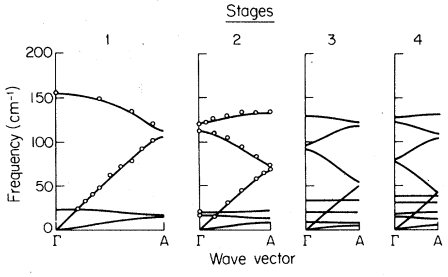

FIG. 5. Phonon-dispersion curves along the ΓA direction in stages 1, 2, 3 and 4 Rb GIC's. The open circles represent the experimental points taken from Ref. 4 and 7.

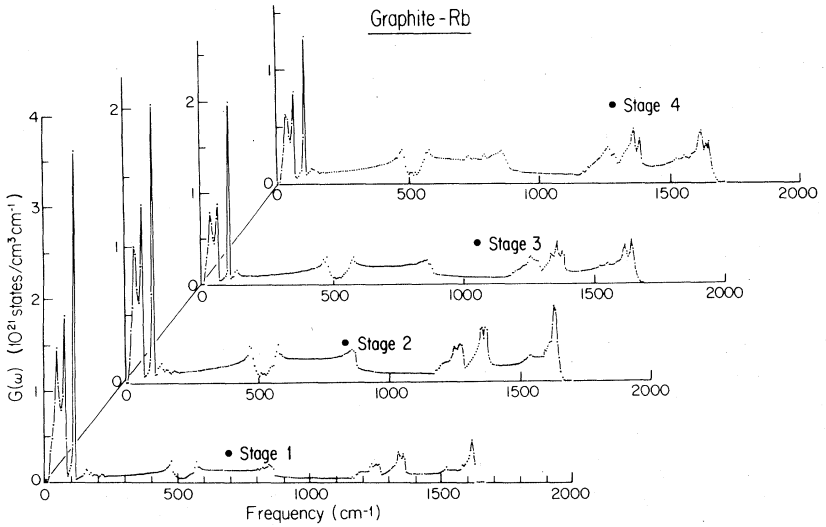

FIG. 6. Phonon density of states for Rb GIC stages $n=1$, 2, 3, and 4 corresponding to the dispersion curves in Fig. 3. Above $\sim 100\ \mathrm{cm}^{-1}$, the phonon density-of-states curves are very similar to pristine graphite. The three sharp features at low frequency arise from low-frequency in-plane shear modes, which sensitively depend on the intercalate layer.

emitted, whereas in second-order Raman processes, two phonons from the same branch (overtones) or from different branches (combination) of opposite wave vectors are emitted.

First- and second-order Raman scattering experiments have been carried out, and particular attention has been given to probe the high-frequency phonon modes in donor GIC's.[14] First-order Raman peaks were observed for all stages with a splitting into two closely spaced peaks for $n \geq 3$.[8–14] On the other hand, peaks in the second-order Raman spectra in the vicinity of $\omega \approx 2450$, 2720, and 3230 cm^{-1} were reported[14] for $n \geq 3$ and none for stages 1 and 2; however, no mode splittings are observed in the second-order spectra in contrast to the case of the first-order Raman spectra. In this section we explain these observations by considering the effect of the charge transfer from the donor layers to the bounding graphite layers on the Raman spectra. By calculating the imaginary part of the phonon self-energy, we shall show that for disordered intercalant layers the phonon bandwidth for the graphite bounding layers is too broad to be observed.

We start by considering the problem of phonon renormalization due to electron-phonon interaction. In terms of the annihilation and creation operators of an electron with wave vector $\vec{k}$, denoted by C_k and $C_k^\dagger$, and the corresponding phonon operators b_q and $b_q^\dagger$, the electron-phonon interaction Hamiltonian is given by

$$H_{\mathrm{int}} = \sum_{\substack{k,q \\ \alpha,\alpha'}} g_{\alpha\alpha'} C^\dagger_{k+q,\alpha'} C_{k,\alpha} (b_q + b^\dagger_{-q}) , \tag{7}$$

where $g_{\alpha\alpha'}$, the matrix element of the interaction, is taken to be wave-vector independent, and α and α' are electron pocket indices. The Dyson equation[39] for the renormalized phonon propagator is illustrated in Fig. 7, which also expresses the phonon self-energy Σ_q in terms of the electron polarization. If we take the Coulomb interaction between electrons into account, then Fig. 7 implies that

$$\Sigma_q = -\frac{2i}{\hbar} \sum_{\alpha,\alpha'} \frac{g^2_{\alpha\alpha'}}{\epsilon(q)} \int \frac{d^4k}{(2\pi)^4} G_\alpha(k) G_{\alpha'}(k-q) , \tag{8}$$

where $G_\alpha(k)$ is the propagator for an electron with

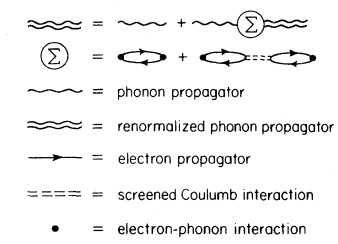

FIG. 7. Renormalized phonon propagator due to electron-phonon interaction. The figure also expresses the phonon self-energy in terms of the electronic polarization.

four-momentum $k=(\vec{k},\omega)$, and $\epsilon(q)$ is the dielectric constant which in the static limit $\epsilon(q)=\epsilon(\vec{q},0)$ is approximated by[40]

$$\epsilon(q)=1+\frac{k_s^2}{|q|^2}u(|\vec{q}|/2k_F) \tag{9}$$

and depends only on the magnitude of the phonon wave vector. In Eq. (9), k_s represents the screening wave vector and k_F the Fermi wave vector, and the kernel is given by[40]

$$u(x)=\frac{1}{2}+\frac{1-x^2}{4x}\ln\left|\frac{1+x}{1-x}\right| . \tag{10}$$

The real part of Σ_q is proportional to a phonon-frequency shift, whereas its imaginary part gives rise to an increase in the phonon bandwidth. From Eq. (8) the imaginary part of the self-energy at zero temperature is given by

$$\mathrm{Im}\Sigma_q=\frac{-1}{(2\pi)^2}\sum_{\alpha,\alpha'}\frac{g_{\alpha\alpha'}^2}{\epsilon(q)}\int d^3k\,\Theta(k_F-k)\Theta(|\vec{k}+\vec{q}-\vec{Q}_{\alpha\alpha'}|-k_F)\delta(\epsilon_\alpha(\vec{k})-\epsilon_{\alpha'}(\vec{k}+\vec{q}-\vec{Q}_{\alpha\alpha'})+\hbar\omega) , \tag{11}$$

where $\vec{Q}_{\alpha\alpha'}$ is the vector connecting the centers of pockets α and α' in the Brillouin zone, and

$$\Theta(x)=\begin{cases}1 & \text{if } x>0\\ 0 & \text{if } x<0\end{cases} \tag{12}$$

denotes the step function. Equation (11) is proportional to the probability of transferring an electron from below the Fermi surface in electron pocket α to above the Fermi surface in pocket α' by a phonon absorption. The δ function expresses energy conservation in this process.

To evaluate $\mathrm{Im}\Sigma_q$, we assume that the electronic Fermi surface is cylindrical about the z axis, yielding the following dispersion relation:

$$\epsilon_\alpha(\vec{k})=\frac{\hbar^2}{2m}(k_x^2+k_y^2) . \tag{13}$$

In the case of the stage-1 compounds, a single-layer model for the graphite with a linear dispersion relation should be used.[41] This was done in the calculation of the phonon-dispersion relations and the phonon density of states presented in Sec. II. For the application of the model to the Raman spectra, we are only interested in identifying the location of Raman structure with specific points in the Brillouin zone and in explaining the origin of certain physical characteristics of the observed first- and second-order Raman spectra. It is thus possible to make a number of simplifying approximations in the calculations relating to the intensity of the first- and second-order Raman spectra that are not critical to the calculated intensities [e.g., the calculated Raman cross sections are not sensitive to the exact form or parameters of Eq. (13)]. Using this assumption, and denoting $\vec{q}-\vec{Q}_{\alpha\alpha'}$ by $\vec{q}\,'$, we obtain three possibilities for $\mathrm{Im}\Sigma_q$:

$$\mathrm{Im}\Sigma_q=(-mk_c/2\hbar^2\pi^2)\sum_{\alpha,\alpha'}(k_{F\perp}/q')[g_{\alpha\alpha'}^2/\epsilon(q)][1-(m\omega/\hbar q'k_{F\perp}-q'/2k_{F\perp})^2]^{1/2}$$
$$\text{if } q'>2k_{F\perp} \text{ and } +(\hbar q'^2+2\hbar q'k_{F\perp})/2m>\omega>(\hbar q'^2-2\hbar q'k_{F\perp})/2m \tag{14a}$$
$$\text{or } q'<2k_{F\perp} \text{ and } (\hbar q'^2+2\hbar q'k_{F\perp})/2m>\omega>(2\hbar q'k_{F\perp}-\hbar q'^2)/2m ,$$

$$\mathrm{Im}\Sigma_q=(-mk_c/2\hbar^2\pi^2)\sum_{\alpha,\alpha'}(k_{F\perp}/q')[g_{\alpha\alpha'}^2/\epsilon(1)]\{[1-(m\omega/\hbar q'k_{F\perp}-q'/2k_{F\perp})^2]^{1/2}$$
$$-[1-(m\omega/\hbar q'k_{F\perp}+q'/2k_{F\perp})^2]^{1/2}\}$$
$$\text{if } q'<2k_{F\perp} \text{ and } 0<\omega<(2\hbar q'k_{F\perp}-\hbar q'^2)/2m , \tag{14b}$$

or

$$\mathrm{Im}\Sigma_q=0 \text{ otherwise} . \tag{14c}$$

In the above equation, k_c is the length of the Fermi surface along the k_z axis and $k_{F\perp}$ is the radial Fermi wave vector. As seen in Eq. (14c), the imaginary part of the self-energy vanishes for a phonon whose wave vector $\vec{q}=\vec{Q}_{\alpha\alpha'}$. We thus conclude that the electron-phonon interaction does not give rise to any decrease in the lifetime of zone-center phonons ($\vec{Q}_{\alpha\alpha}=0$), a result which directly follows from the requirement that both wave vector and energy must

be conserved. On the other hand, for phonons with large wave vectors [Eq. (14a)], the dielectric constant becomes $\epsilon(q)\sim 1$, giving a negligible screening of the electron-phonon interaction due to electronic polarization. The imaginary part of the self-energy is negligible as long as $|\vec{q}-\vec{Q}_{\alpha\alpha'}| \gg 2k_{F\perp}$, a situation that applies in pristine graphite to phonon modes away from the zone-center except for those in the immediate vicinity of the K point where $\mathrm{Im}\Sigma_q$ vanishes anyway, as seen in Eq. (14c). If the electronic density is sufficiently large so that $2k_{F\perp}\sim |\vec{q}-\vec{Q}_{\alpha\alpha'}|$, then $\mathrm{Im}\Sigma_q$ will assume a value mainly determined by $g_{\alpha\alpha'}$, the unscreened interaction matrix element for both intrapocket and interpocket scattering of electrons by phonon absorption. In such a case, the phonon lifetime could be sufficiently short so that the width of a second-order Raman line, which is an overtone of such a phonon mode, would be sufficiently large to make the Lorentzian peak amplitude of the phonon too small to be detected.

Upon intercalation, the electronic density in the carbon layers bounding the intercalate layers is several hundred times larger than that before intercalation. On the other hand, the electronic density is only slightly modified in the graphite interior layers. According to the above discussion, this large increase in the density of electrons in the graphite bounding layers leads to negligible damping effects for zone-center phonons. Thus, the above discussion shows why it is possible to observe the first-order Raman spectrum for all stages of donor GIC's. The graphite bounding-layer phonon modes away from the zone-center, however, are highly damped, and thus it is hard to observe any features in the second-order Raman spectrum that arise from such phonons. Assuming that $k_{F\perp}\approx 3\times 10^7$ cm^{-1}, we see from Eqs. (14a) and (14b) that phonons along the ΓK direction giving rise to peaks in the density of states at ~ 1620 and ~ 1350 cm^{-1} acquire bandwidths of few hundred cm^{-1} for an electron-phonon matrix element $g_{\alpha\alpha'}$ of ~ 1.0 eV normalized to a unit-cell volume. In the situation where we have cylindrical electron pockets at the equivalent K points in the Brillouin zone, however, the M-point phonons are not damped, and a peak in the second-order Raman spectrum at ~ 2720 cm^{-1} should be observable. The M-point phonons are probably damped by electron-phonon scattering in which electrons in the cylindrical pockets are scattered into the spherical pocket centered at the Γ point and which results from the s electrons of the intercalate layer, as well as intra-s pocket electron scattering through phonon absorption. Accordingly, the absence of a peak in the second-order spectrum of stage-2 alkali-metal compounds is an indication of an occupation of the s band for that stage. The disordered intercalate layer also provides a mechanism for damping the second-order Raman modes associated with the bounding layer.

An appreciable filling of the electronic conduction bands imposes phase-space limitations on electron-hole creation through photon absorption and electron scattering in the conduction band with phonon emission. Since both virtual processes occur in a second-order Raman scattering event, a resultant decrease in the cross section of the scattered light is predicted.

Summarizing our results so far, we note that while the first-order Raman spectrum may be observed for light scattering from phonons identified with carbon-atom vibrations in graphite interior layers, or those bounding the intercalate, second-order Raman features can only be observed from phonons that describe the atomic vibrations in the graphite interior layers in the case of donor intercalants such as K, Rb, or Cs; the contributions to the second-order spectra from the graphite bounding layers are too heavily damped to be observable.

B. Calculations of the second-order Raman spectra

In second-order Raman scattering, the incident photon is annihilated, a scattered photon is created, and two phonons are emitted or absorbed, or one is emitted and the other is absorbed. The photon-phonon interaction takes place via the electron-photon and electron-phonon interactions. The second-order Raman cross section for Stokes processes (two phonons are emitted) is given by

$$\frac{d^2\sigma}{d\Omega\, d\omega'} = \sum_{i,q} W(\vec{q},i)\delta(\omega-\omega'-2\omega_i(\vec{q}))\ , \tag{15}$$

where $\vec{q}$, i, and $\omega_i(\vec{q})$ denote the phonon wave vector, branch, and frequency, respectively, and ω and ω' are, respectively, the frequencies of the incident and scattered photons. The scattering cross section is thus a weighted density of states in which the weight function $W(\vec{q},i)$ is proportional to the square of the second-order Raman tensor. We follow the same assumptions as in the case of pristine graphite,[31,32] so that the weight function is taken to be proportional to the fourth power of electron-

phonon interaction matrix element, and the electron—LA-phonon coupling constant is taken to be 3.5 times larger than the electron—optic-phonon coupling constant. These assumptions were shown to yield a calculated second-order Raman spectrum for pristine graphite that reproduced all the main features in the experimentally observed spectrum: the peak positions as well as their relative intensities.[32] Since in the case of alkali-metal GIC's, contributions to the second-order Raman spectrum come only from graphite interior layers, which to a good approximation are unaffected by the intercalation process, it is expected that the same assumptions concerning the electron-phonon interactions in pristine graphite will hold in the case of alkali-metal GIC's. It should be noted that the electron scattering by phonon emission or absorption that is discussed here in connection with the second-order Raman spectrum is not the same as that giving rise to phonon damping. While the processes that lead to the broadening of the phonon bandwidth are real absorption or emission processes that involve free carriers and which are energy conserving, those determining the Raman cross section are virtual processes in which no free carriers participate.

In general, the phonon modes at general points in the Brillouin zone are not purely optic or acoustic, transverse or longitudinal, but rather have a mixed character. In stage-3 GIC's, we determine the 21-component normalized eigenvector $V(\vec{q},i)$, $1 \leq i \leq 21$, at many points in the Brillouin zone, and then project these eigenvectors along those for the zone-center phonon modes. According to the discussion in Sec. III A, the bounding-layer phonon contributions to the second-order Raman scattering cannot be observed because of strong damping effects; thus the calculated eigenvectors are projected along the eigenvectors for the phonons associated with the graphite interior layer only. The probabilities P_l^2 and P_o^2 that the phonon is either a graphite interior layer longitudinal-acoustic or an optical phonon corresponding to atomic in-plane vibrations of the graphite layer are given by

$$P_l^2(\vec{q},i)=\{[V_1(\vec{q},i)+V_4(\vec{q},i)]q_x+[V_2(\vec{q},i)+V_5(\vec{q},i)]q_y\}^2/2\,|\,\vec{q}\,|^2\,, \tag{16}$$

$$P_o^2(\vec{q},i)=[\,|\,V_1(\vec{q},i)-V_4(\vec{q},i)\,|^2+|\,V_2(\vec{q},i)-V_5(\vec{q},i)\,|^2]/2\,, \tag{17}$$

where the first six rows and columns of the 21×21 dynamical matrix are identified with the two distinct atoms in the graphite interior layer. For stage-4 GIC's, we identify the first 12 rows and columns of the 27×27 dynamical matrix with the four distinct carbon atoms in the two graphite interior layers. The corresponding probabilities for a phonon to be an in-plane interior-layer longitudinal-acoustic or an optic phonon are, respectively, given by

$$P_l^2(\vec{q},i)=|\,q_xT_x(\vec{q},i)+q_yT_y(\vec{q},i)\,|^2/|\,\vec{q}\,|^2 \tag{18}$$

and

$$\begin{aligned}P_o^2(\vec{q},i)=\tfrac{1}{4}\sum_{j=1,2}[\,&|\,V_j(\vec{q},i)+V_{j+3}(\vec{q},i)-V_{j+6}(\vec{q},i)-V_{j+9}(\vec{q},i)\,|^2\\&+|\,V_j(\vec{q},i)-V_{j+3}(\vec{q},i)-V_{j+6}(\vec{q},i)+V_{j+9}(\vec{q},i)\,|^2\\&+|\,V_j(\vec{q},i)-V_{j+3}(\vec{q},i)+V_{j+6}(\vec{q},i)-V_{j+9}(\vec{q},i)\,|^2]\,,\end{aligned} \tag{19}$$

where the three-component vector $\vec{T}(\vec{q},i)$ is related to components of the 27-component normal mode vector $\vec{V}(\vec{q},i)$ by

$$T_j(\vec{q},i)=\sum_{n=0,3}V_{j+3n}(\vec{q},i)/2,\quad j=1,2,3\,. \tag{20}$$

As in the case of the calculation of the second-order Raman spectrum in pristine graphite,[31,32] the weight function $W(\vec{q},i)$ is chosen to contain an additional wave-vector—dependent term that reflects the symmetry of the crystal. The form thus obtained for the weight function is

$$W(\vec{q},i)=F(\vec{q})[P_o^2(\vec{q},i)+3.5P_l^2(\vec{q},i)]^4 \tag{21}$$

in which $F(\vec{q})$ has the same functional form as in the pristine graphite calculation, so that

$$F(\vec{q})=(1+F_{10}+2.65F_{20}-3.5F_{21})^2 \tag{22}$$

and the wave-vector–dependent symmetrized functions are[42]

$$\begin{aligned} F_{10}&=\{\cos(2\pi k_1/3)+\cos[2\pi(k_1+k_2)/3]+\cos(2\pi k_2/3)\}/3\ , \\ F_{20}&=\{\cos(4\pi k_1/3)+\cos[4\pi(k_1+k_2)/3]+\cos(4\pi k_2/3)\}/3\ , \\ F_{21}&=\{\cos[2\pi(2k_1+k_2)/3]+\cos[2\pi(k_1+2k_2)/3]+\cos[2\pi(k_1-k_2)/3]\}/3\ . \end{aligned} \tag{23}$$

Finally, we take into account the phonon bandwidth in the calculation of the second-order Raman spectrum. The δ function in Eq. (15) implies that the phonon mode has zero bandwidth and thus an infinite lifetime. To incorporate into the calculation the finiteness of phonon lifetimes, the δ function is replaced by a Lorentzian distribution centered at the phonon frequency $\omega_i(\vec{q})$. Consequently, the Raman scattering cross section that we calculate has the form

$$\frac{d^2\sigma}{d\omega' d\Omega}=\sum_{q,i}\frac{W(\vec{q},i)}{4\{[(\omega-\omega')/2-\omega_i(q)]^2+\Gamma^2\}} \tag{24}$$

where Γ is taken to be 6 cm^{-1}, and $W(\vec{q},i)$ is given in Eq. (21). We note that the expression for the cross section as given in Eqs. (15) and (24) assumes that the two emitted phonons have equal and opposite wave vectors and are on the same branch of the dispersion curves. In Fig. 8 we plot the second-order Raman intensity of a stage-3 and a stage-4 Rb GICs as calculated from Eq. (24) according to the assumptions made in Eq. (21). These plots show good agreement between the calculated peak positions and the experimentally reported ones.[14]

The main features in the calculated spectra for both stage-3 and stage-4 Rb GIC's at frequencies $\omega\approx 3220$ and 2700 cm^{-1}, respectively, arise from the maximum in the phonon-dispersion curves along the ΓK direction and the region near the M

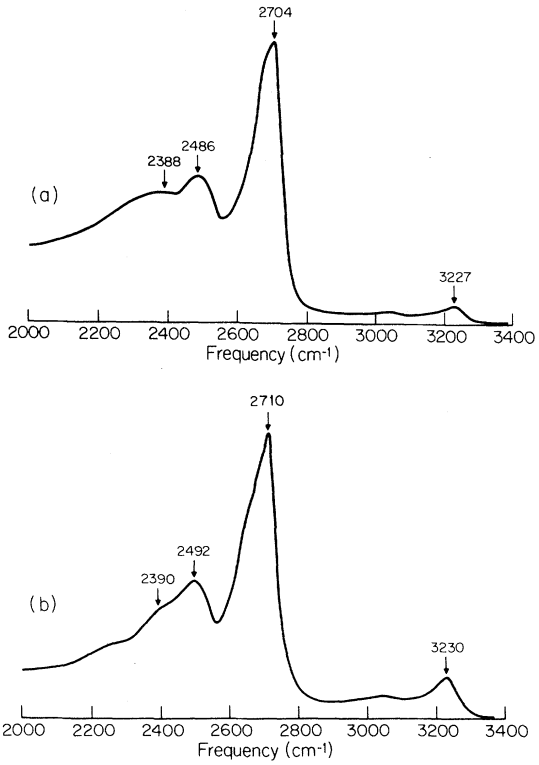

FIG. 8. Calculated second-order Raman spectra for (a) stage-3 Rb GIC's and (b) stage-4 Rb GIC's according to Eq. (24). The calculated spectra explain the main features observed experimentally.

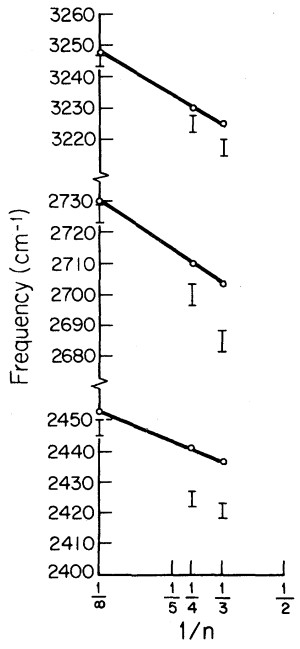

FIG. 9. Positions of the peaks in the second-order Raman spectrum in Rb GIC's as a function of the reciprocal of the stage index. The open circles represent the calculated values and the error bars indicate the experimentally observed values according to Ref. 14.

point. The peak at $\omega \approx 3220$ cm^{-1} is identified with optic phonons, while that at $\omega \approx 2700$ cm^{-1} results from longitudinal-acoustic phonons (see Fig. 3). The doublet at $\omega \approx 2410$ and 2500 cm^{-1} arises from midzone minima and maxima in the phonon-dispersion curves resulting from the coupling of the optic and longitudinal-acoustic phonon branches. Such a coupling gives peaks in the density of states that are rich in longitudinal-acoustic character which couples strongly to the electrons and holes, causing an appreciable scattering cross section at the corresponding frequencies.

A comparison between the peak frequencies of the experimentally observed features and the results of the calculation are shown in Fig. 9 for the second-order Raman spectrum as a function of the reciprocal of the stage index. As shown in this figure, the calculation gives a stage-dependent shift in the positions of the peaks of the second-order Raman spectrum. This results from the stage dependence of the force constants for vibrations in the graphite interior layers, given in Eq. (2). The calculation, however, does not account for the whole frequency shift that is observed experimentally. One possible explanation is that there is a small frequency shift resulting from the real part of the self-energy. Although the charge transferred to the interior graphite layers is only a small fraction of that transferred to the bounding graphite layers, the additional charge in the graphite interior layers could be large enough to cause a small downward frequency shift for phonons whose wave vectors are away from the zone center [$\epsilon(q) \sim 1$ for such phonons]. That such a shift is downward can be mathematically shown in some simple cases, such as a spherical Fermi surface.[39] We assume that the

TABLE VII. Comparison for K GIC's between various experimental values and the model presented in this paper.

Material Stage	X	Type of experiment	Mode symmetry	Value (cm^{-1}) Expt.	Model	Ref.
1	K	Elastic neutron scattering[a]	Γ	~201	201	3
			A	~120	111	3
			A	~170	170	3
2	K	Raman (first order)	Γ	~19	19	15
			Γ	~23	23	15
			Γ	~1600	1600	34
		Elastic neutron scattering[b]	Γ	~115	115	3
			Γ	~180	180	3
			A	~73	73	3
			A	~86	83	3
			A	~180	180	3
3	K	Raman (first order)	Γ	~23	23	15
			Γ	~33	34	15
		Elastic neutron scattering[c]	Γ	~95	96	15
			Γ	~105	105	3
			Γ	~180	175	3
			A	~53	53	3
			A	~58	58	3
			A	~120	120	3
			A	~180	175	3
4	K	Raman (first order)	Γ	~16	18	15
			Γ	~19	19	15
			Γ	~39	39	15

[a]The residual (χ^2) error of the mode to 17 points was less than 5%.
[b]The residual (χ^2) error of the mode to 16 points was less than 5%.
[c]The residual (χ^2) error of the mode to 26 points was less than 5%.

same will hold in the case of a cylindrical Fermi surface.

IV. CONCLUSIONS

The calculation presented in this work is easily extended to any stage index by virtue of the fact that we only make use of the k_z-axis zone-folding technique. The results of this calculation for stage-1, -2, -3, and -4 of Rb, K, and Cs GIC's are in good agreement with all the reported experimental values on the lattice properties of these compounds shown in Tables VII–IX. The calculation reproduces the observed high- and low-frequency Raman-active modes as well as the dispersion curves measured by neutron scattering from the [001] longitudinal phonons (see Figs. 4 and 5). The calculations also account for the mode frequencies indentified with intercalate planar atomic vibrations through neutron scattering and specific-heat measurements (see Figs. 3 and 6). The classification of the graphite layers into interior and bounding layers and the assumption that most of the charge transferred from the intercalate layer to the graphite layers resides on the carbon bonding layers allow us to explain why the second-order Raman spectrum is difficult to observe in stages $n=1$ and 2. Graphite interior layers exist only when $n \geq 3$, for which case the second-order Raman peaks become observable. The

TABLE VIII. Comparison for Rb compounds betwen various experimental values and the model presented in this paper.

Material Stage	X	Type of experiment	Mode symmetry	Value (cm^{-1}) Expt.	Model	Ref.
1	Rb	Elastic neutron scattering[a]	Γ	~155	155	1
		Specific-heat anomaly		~49	46	21–23
2	Rb	Raman (first order)	Γ	~17	17	7
			Γ	~21	20	7
			Γ	~1600	1600	14
		Elastic neutron scattering[b]	Γ	~112	112	3
			Γ	~120	120	3
			A	~72	72	3
			A	~68	68	3
			A	~134	132	3
		Specific-heat anomaly		~35	35	21–23
3	Rb	Raman (first order)	Γ	~1578	1578	14
			Γ	~1603	1605	14
		Raman (second order)		~2420	2437	14
				~2685	2704	14
				~3220	3227	14
		Specific-heat anomaly		~35	35	22
4	Rb	Raman (first order)	Γ	~1579	1579	14
			Γ	~1607	1608	14
		Raman (second order)		~2425	2441	14
				~2700	2710	14
				~3225	3230	14
		Specific-heat anomaly		~35	38	22

[a]The residual (χ^2) error of the mode to 13 points was less than 2%.
[b]The residual (χ^2) error of the mode to 19 points was less than 2%.

TABLE IX. Comparison for Cs compounds between various experimental values and the model presented in this paper.

Material Stage	X	Type of experiment	Mode symmetry	Value (cm^{-1}) Expt.	Model	Ref.
1	Cs	Elastic neutron scattering[a]	Γ	~140	140	3
			A	~82	90	3
			A	~120	106	3
		Specific-heat anomaly		~33	36	21
2	Cs	Raman (first order)	Γ	~1600	1600	34
		Elastic neutron scattering[a]	Γ	~112	112	3
			A	~68	68	3
			A	~120	121	3
		Specific-heat anomaly		~24	28	21
3	Cs	Raman (first order)	Γ	~1603	1605	34
		Specific-heat anomaly		~24	28	21
4	Cs	Specific-heat anomaly		~24	28	21

[a]The residual (χ^2) error of the mode to 16 points was less than 5%.

second-order Raman cross section for GIC's is calculated for stages 3 and 4, employing the same assumptions as were previously applied to the case of pristine graphite, and all the main features in the observed spectrum are reproduced in the correct positions (see Fig. 8).

ACKNOWLEDGMENTS

We wish to thank Professor M. S. Dresselhaus and Professor P. C. Eklund for valuable discussions and AFOSR Contract No. F49620-81-C-0006 for support.

[1]W. D. Ellenson, D. Semmingsen, D. Guérard, D. G. Onn, and J. E. Fischer, Mater. Sci. Eng. 31, 137 (1977).

[2]A. Magerl and H. Zabel, Phys. Rev. Lett. 46, 444 (1981).

[3]A. Magerl and H. Zabel, in *Physics of Intercalation Compounds,* Vol. 38 of *Springer Series of Solid State Sciences,* edited by L. Pietronero and E. Tosatti (Springer, Berlin, 1981), p. 180.

[4]H. Zabel and A. Magerl, in *Proceedings of the International Conference on Phonon Physics, Bloomington, Indiana, 1981,* edited by W. E. Bron, (Editions de Physique, Paris, 1981).

[5]W. A. Kamitakahara, N. Wada, and S. A. Solin, *Proceedings of the International Conference on Phonon Physics, Bloomington, Indiana, 1981,* Ref. 4.

[6]P. C. Eklund, J. Giergiel, and P. Boolchand, in *Physics of Intercalation Compounds,* Vol. 38 of *Springer Series in Solid State Sciences,* Ref. 3, p. 168.

[7]J. Giergiel, P. C. Eklund, R. Al-Jishi, and G. Dresselhaus (unpublished).

[8]J. J. Song, D. D. L. Chung, P. C. Eklund, and M. S. Dresselhaus, Solid State Commun. 20, 1111 (1976).

[9]R. J. Nemanich, S. A. Solin, and D. Guérard, Phys. Rev. B 16, 2965 (1977).

[10]C. Underhill, S. Y. Leung, G. Dresselhaus, and M. S. Dresselhaus, Solid State Commun. 29, 769 (1979).

[11]S. A. Solin, Mater. Sci. Eng. 31, 153 (1977).

[12]S. Y. Leung, D. Dresselhaus, and M. S. Dresselhaus, Synth. Met. 2, 89 (1980).

[13]S. A. Solin, Phys. Rev. B 24, 6083 (1981); Physica (Utrecht) 99B, 443 (1980).

[14]G. Giergiel, P. C. Eklund, and C. Underhill, in *Extended Abstracts of the Fifteenth Biennial Conference on Carbon, Philadelphia, Pennsylvania, 1981,* edited by W. C. Forsman, p. 46.

[15]N. Wada, M. V. Klein, and H. Zabel, in *Physics of Intercalation Compounds,* Vol. 38 of *Springer Series in Solid State Sciences,* Ref. 3, p. 199.

[16]P. Boolchand, W. J. Bresser, D. McDaniel, V. Yeh, and P. C. Eklund (unpublished).

[17]P. C. Eklund, G. Dresselhaus, M. S. Dresselhaus, and J. E. Fischer, Phys. Rev. B 16, 3330 (1977).

[18]M. S. Dresselhaus, G. Dresselhaus, P. C. Eklund, and D. D. L. Chung, Mater. Sci. Eng. 31, 141 (1977).

[19]P. C. Eklund and K. R. Subbaswammy, Phys. Rev. B 20, 5157 (1979).

[20]H. Miyazaki, T. Hatano, G. Kusunoki, T. Watanabe, and C. Horie, Physica (Utrecht) 105B, 381 (1981).

[21]U. Mizutani, T. Kondow, and T. B. Massalski, Phys. Rev. B 17, 3165 (1978).

[22]M. Suganuma, T. Kondow, and U. Mizutani, Phys. Rev. B 23, 706 (1981).

[23]M. G. Alexander, D. P. Goshorn, and D. G. Onn, Phys. Rev. B 22, 4535 (1980).

[24]C. Horie, M. Maeda, and Y. Kuramoto, Physica (Utrecht) 99B, 430 (1980).

[25]M. Maeda, Y. Kuramoto, and C. Horie, J. Phys. Soc. Jpn. 47, 337 (1979).

[26]S. Y. Leung, G. Dresselhaus, and M. S. Dresselhaus, Phys. Rev. B 24, 6083 (1981).

[27]J. E. Fischer, in *Physics and Chemistry of Materials with Layered Structures,* edited by F. Lévy (Reidel, Dordrecht, 1979), Vol. 6, p. 481.

[28]J.-P. Issi, J. Heremans, and M. S. Dresselhaus, *Physics of Intercalation Compounds,* Vol. 38 of *Springer Series in Solid State Sciences,* Ref. 3, p. 310.

[29]P. C. Eklund, D. S. Smith, V. R. K. Murthy, and S. Y. Leung, Synth. Met. 2, 99 (1980).

[30]A. Erbil, G. Dresselhaus, and M. S. Dresselhaus, Phys. Rev. B 25, 5451 (1982).

[31]R. Al-Jishi, B. S. Elman, and G. Dresselhaus, in *Extended Abstracts of the Fifteenth Biennial Carbon Conference, Philadelphia, Pennsylvania, 1981,* Ref. 14, p. 34.

[32]R. Al-Jishi and G. Dresselhaus, preceding paper, Phys. Rev. B 26, 4514 (1982).

[33]M. S. Dresselhaus and G. Dresselhaus, in *Physics and Chemistry of Materials with Layered Structures,* Ref. 27, p. 423; Adv. Phys. 30, 139 (1981).

[34]M. S. Dresselhaus and G. Dresselhaus, in *Light Scattering in Solids,* Vol. 51 of *Topics in Applied Physics,* edited by M. Cardona and G. Güntherodt (Springer, Berlin, 1982), p. 3.

[35]A. Herold, in *Physics and Chemistry of Materials with Layered Structures,* Ref. 27, p. 323.

[36]L. Pietronero and S. Straessler, Phys. Rev. Lett. 47, 593 (1981).

[37]D. E. Nixon and G. S. Parry, J. Phys. C 2, 1732 (1969).

[38]G. Gilat and L. J. Raubenheimer, Phys. Rev. 144, 390 (1966).

[39]A. A. Abrikosov, L. P. Gorkov, and I. E. Dzyloshinsky, *Methods of Quantum Field Theory in Statistical Physics* (Dover, New York, 1975).

[40]J. Lindhard, K. Dansk. Vidensk. Selsk. Mat. Fys. Medd. 28, 8 (1954).

[41]M. S. Dresselhaus and G. Dresselhaus, Adv. Phys. 30, 139 (1981).

[42]L. G. Johnson and G. Dresselhaus, Phys. Rev. B 7, 2275 (1973).